Visual Servoing-Based Anti-Swing Control of Cable-Suspended Aerial Transportation Systems With Variable-Length Cable

Hai Yu , *Student Member, IEEE*, Zhaopeng Zhang , Tengfei Pei, Jianda Han , *Member, IEEE*, Yongchun Fang , *Senior Member, IEEE*, and Xiao Liang , *Member, IEEE*

Abstract— By utilizing a suspension cable to connect the payload with the quadrotor, transport tasks can be accomplished while preserving the unmanned aerial vehicle's agility and maneuverability, particularly in environments that are impassable for ground vehicles. Equipping onboard visual sensors and utilizing image-based visual servoing techniques, the application range of aerial transportation systems is poised to be significantly expanded in scenarios like autonomous landing and goods release. Unfortunately, within the system, there exist multiple layers of dynamic couplings between image features, quadrotor rotation, translation, and payload motion. These intricacies give rise to numerous difficulties in achieving smooth anti-swing transportation. To overcome the aforementioned difficulties, this paper presents the first image-based visual servoing control scheme for the aerial transportation system with variable-length cable. Specifically, the image moments defined on the rotated virtual image plane are taken as the image features, whose dynamics is independent of the quadrotor rotational motion. Subsequently, a generalized virtual image feature signal is introduced by organically combining the cable length and payload swing angles with the image feature, which is further exploited in the anti-swing control scheme design. The equilibrium point of the overall closed-loop system is proved to be asymptotically stable through Lyapunov techniques and LaSalle's Invariance Theorem. Hardware experiments are conducted on a self-built aerial transportation platform to verify the proposed controller's basic and functional performance in terms of rapid anti-swing and accurate target position and cable length tracking.

Note to Practitioners—This paper is motivated by the requirement to improve the autonomy level and payload swing suppression ability of the aerial transportation system through visual servoing techniques. By installing onboard monocular cam-

era and the cable length adjustment mechanism, the application scope of the aerial transportation system can be significantly expanded. However, due to the "double" underactuated characteristic, the visual features couple with both the quadrotor motion and the payload motion, hence, it is quite challenging to realize visual servoing control for cable-suspended aerial transportation systems with simultaneous payload swing suppression and quadrotor positioning. Accounting for the foregoing problems, this paper proposes an image-based visual servoing anti-swing control scheme. With the elaborately constructed generalized virtual image feature signal, the designed controller could improve the anti-swing ability with a completed theoretical analysis. Furthermore, two groups of hardware experiments are conducted to validate the effectiveness of the suggested control method. In future studies, we intend to design more effective control scheme for payload delivery issue with consideration of the visibility of the mobile platform.

Index Terms— Aerial transportation systems, image-based visual servoing, variable-length cable, payload swing elimination.

I. INTRODUCTION

WITH the rapid advance in mechanics and electronics [1], [2], [3], [4], [5], [6], [7], robotics technology has driven the development of various fields such as the military, industry, agriculture, entertainment, and transportation, etc. Specifically, in the field of intelligent transportation, thanks to the three-dimensional (3D) movement capability of flying robots, a great convenience for cargo delivery under complex road and terrain conditions is provided. As one of the aerial transportation means, the cable-suspended way has received widespread attention due to its adaptability to various scenarios and high cost-effectiveness.

Recently, researchers have conducted extensive studies from both control and planning perspectives to complete cable-suspended payload transportation [8], [9], [10], [11], [12], [13]. Zeng et al. propose a nonlinear geometric control law [8] based on the established coordinate-free quadrotor-pulley-load dynamics model, which has the ability to track quadrotor attitude, payload attitude and position, and cable length. To deal with external disturbance, a fixed-time control strategy [9] is developed to improve the transient response and robustness of the cable-suspended aerial transportation system. Meanwhile, considering the presence of unknown air

turbulence, a robust control scheme [10] is designed based on the robust integral of the sign of the error (RISE). To pass through windows and avoid obstacles, an aggressive payload position and swing angle trajectory generation approach is designed in [11], which embeds constraints for cable direction into the trajectory generation process. Employing the complementarity constraints and reformulating the obstacle avoidance from nonconvex constraints into smooth ones, a planning method is designed to generate agile quadrotor motions in [12]. Based on Pontryagin's Minimum Principle, the optimal quadrotor trajectory and cable length are generated in [13], which has the ability to improve the carrying capacity and reduce the oscillation of the payload.

Currently, the lightweight onboard monocular cameras are becoming increasingly popular, which can provide rich information at a low cost and have been widely employed to acquire the motion information of quadrotors through position-based visual servoing (PBVS) method [14], [15], [16], [17] and image-based visual servoing (IBVS) method [18], [19], [20], [21]. PBVS method is utilized to reconstruct the relative pose between the quadrotor and the target, which is intuitive in Cartesian space, while the computation burden may be raised. Different from PBVS method, IBVS method is computation friendly, which does not need priori target geometry information, but uses image feature errors on the image plane to generate control signals directly. Besides, IBVS method is insensitive to calibration errors and noise [22], which is more suitable for low-cost quadrotors. However, due to the unknown camera depth as well as the underactuated characteristic and nonlinearity of quadrotors, it is challenging to apply IBVS directly to quadrotor systems. To overcome the aforementioned difficulties, the spherical projection-based approach [23], [24] and the virtual camera approach [25], [26], [27] are utilized to obtain decoupled image feature dynamics. Without estimating parameters related to the unknown height, a spherical projection-based IBVS method is proposed in [23], which can land the quadrotor on a specific moving target even under disturbances. Based on the unified-spherical model, a framework containing image-based estimation, aggressive-maneuvering trajectory generation, and motion control is presented in [24] for multiple windows flight crossing. To solve the problem of undesired behavior in the vertical axis of the spherical projection method, the circle feature [25] is exploited in the virtual camera approach to land the quadrotor on an unpredictable mobile platform. In [26], a forward-looking camera is fixed on the quadrotor to track and monitor the arbitrary flight target in 3D space by projecting the intruder's center point onto a virtual image plane. By exploiting the virtual reticle image plane, a finite-time dynamic visual servoing control scheme [27] is designed to land the quadrotor onto a tilting and moving ground vehicle.

In summary, by employing the direct measurement signals from the onboard camera and utilizing them for visual servoing control, the autonomy level of aerial transportation systems can be further enhanced. Noteworthily, although many researchers have discussed the visual servoing of the quadrotor itself, few studies concentrate on the visual servoing of aerial transportation systems. Compared with the single quadrotor, the visual servoing control of the aerial transportation system with variable-length cable is much more challenging. To sum up, the following crucial problems are listed as:

1) The aerial transportation system presents much more complex underactuated characteristics due to the "double" underactuated characteristic, which is caused by the coupling between the quadrotor translation and rotation, as well as the coupling between the payload motion and quadrotor motion.

2) By employing a cable with adjustable length, the payload can be hoisted or lowered, which effectively extends the system's application range. However, it also exhibits stronger nonlinearity, higher degrees of freedom (DOFs) and more complex dynamic coupling due to the variable-length cable dynamics.

3) The visual features couple with both the quadrotor motion and the payload motion.

To overcome the aforementioned difficulties, this paper proposes the first image-based visual servoing control strategy for the aerial transportation system with variable-length cable. Specifically, the rotated virtual image plane is employed to obtain the image feature, based on which, a generalized virtual image feature signal containing both payload swing angles and cable length information is incorporated into the control scheme to enhance the payload swing suppression performance. Lyapunov techniques and LaSalle's Invariance Theorem are utilized to guarantee the stability of the overall closed-loop system. Finally, the convincing performance of the proposed method is demonstrated on the self-build experimental testbed. The main contributions of this paper can be summarized as follows:

1) By adopting the rotated virtual image plane, the kinematics of the image feature is decoupled from the rotational motion of the quadrotor. Then, based on the kinematics of the image moment, the dynamic relationship between image feature, cable length, and payload swing angles is established. Thus, the image feature can be successfully integrated into the hierarchical control structure of the aerial transportation system, which brings great convenience to the controller design.

2) By combining the payload swing angles and cable length information, a generalized virtual image feature signal is elaborately constructed for controller design. The proposed controller can not only effectively suppress the payload swing angles, but also ensure the stability of the closed-loop system theoretically.

3) The obtained experimental results show that the proposed method can realize simultaneous target position tracking, cable length adjustment, and payload swing angle elimination. Even if the target point is moving, precise target tracking can be achieved, which further validates the practicality and robustness of the proposed method.

The remainder of this paper is structured in the following manner. The system modeling and problem statements
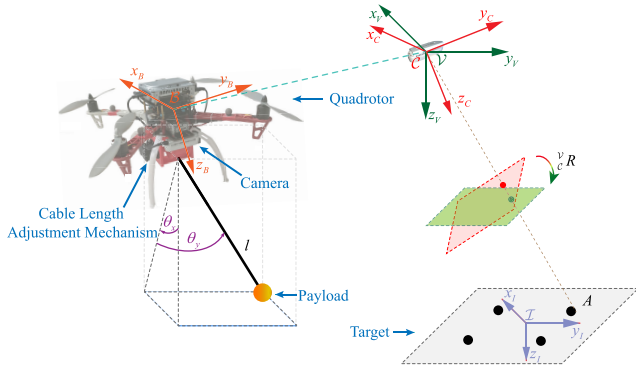
Fig. 1. Geometry relationship between the real image plane, the virtual image plane, and the target plane.

are introduced in Section II. The controller design process, as well as the stability analysis, is provided in Section III. In Section IV, several groups of experimental results are provided to show the performance of the control scheme. Finally, Section V summarizes the paper and presents the feature work.

II. PROBLEM FORMULATION

A. Notations

This part illustrates the symbols utilized in this paper. C_* and S_* denote the abbreviations of $\cos(\theta_*)$ and $\sin(\theta_*)$, respectively. The hat map $\hat{\boldsymbol{w}} : \mathbb{R}^3 \to \mathfrak{so}(3)$ is defined by the relation that $\hat{\boldsymbol{w}}\boldsymbol{p} = \boldsymbol{w} \times \boldsymbol{p}$ for all $\boldsymbol{w}, \boldsymbol{p} \in \mathbb{R}^3$. The vee map $(\cdot)^\vee : \mathfrak{so}(3) \to \mathbb{R}^3$ is the inverse operation of the hat map. For a vector $\boldsymbol{h} \in \mathbb{R}^n$, define $\text{Cosh}(\boldsymbol{h}) = [\cosh(h_1), \ldots, \cosh(h_n)]^\top$, $\text{Tanh}(\boldsymbol{h}) = [\tanh(h_1), \ldots, \tanh(h_n)]^\top$, $\text{Ln}(\boldsymbol{h}) = [\ln(h_1), \ldots, \ln(h_n)]^\top$, and $\text{diag}(\boldsymbol{h})$ is the diagonal matrix with diagonal elements of $h_1, \ldots, h_n$.

The schematic configuration of the visual-based aerial transportation system is shown in Fig. 1. $\mathcal{I}$, $\mathcal{B}$, $\mathcal{C}$ and $\mathcal{V}$ represent the inertial frame, the body-fixed frame, the camera frame, and the virtual camera frame, respectively. Define $_\mathcal{C}^\mathcal{I}R \in SO(3)$ as the rotation matrix from $\mathcal{C}$ to $\mathcal{I}$, and $R \in SO(3)$ as the rotation matrix from $\mathcal{B}$ to $\mathcal{I}$. The camera is fixed on the quadrotor. Thus, the transformation between the camera frame and the body-fixed frame is a constant matrix. After reasonable installation and translation transformation, the camera frame can be viewed as coinciding with the body-fixed frame, i.e., $_\mathcal{C}^\mathcal{I}R = R$. Since the rotated virtual image plane $\mathcal{V}$ is always parallel to the target plane, the rotation matrix from $\mathcal{V}$ to $\mathcal{I}$ can be expressed as $_\mathcal{V}^\mathcal{I}R = I$, where $I \in \mathbb{R}^{3 \times 3}$ is a unit matrix. Thus, the rotation matrix from $\mathcal{C}$ to $\mathcal{V}$ is derived by $_\mathcal{C}^\mathcal{V}R = \left(_\mathcal{V}^\mathcal{I}R\right)^\top {}_\mathcal{C}^\mathcal{I}R = {}_\mathcal{C}^\mathcal{I}R = R$. The symbols and the definitions are listed in TABLE I. Considering the actual transportation systems, as well as the recent researches [8], [9], [10], [11], [12], [28], [29], [30], the following reasonable assumptions are given as follows:

Assumption 1: The payload is always under the quadrotor, implying that the swing angles θ_x and θ_y are within the range of $(-\pi/2, \pi/2)$.

TABLE I
SYMBOLS AND DEFINITIONS OF THE SYSTEM

Symbol	Definition
$M \in \mathbb{R}$	Mass of quadrotor
$m \in \mathbb{R}$	Mass of payload
$g \in \mathbb{R}$	Gravitational acceleration
$J \in \mathbb{R}^{3\times3}$	Quadrotor's moment of inertia
$R \in SO(3)$	Rotation matrix from $\mathcal{B}$ to $\mathcal{I}$
$\boldsymbol{\Omega} \in \mathbb{R}^3$	Angular velocity of quadrotor in $\mathcal{B}$
$\boldsymbol{\xi} = [x, y, z]^\top \in \mathbb{R}^3$	Quadrotor position in $\mathcal{I}$
$\boldsymbol{v} = \dot{\boldsymbol{\xi}} \in \mathbb{R}^3$	Quadrotor velocity in $\mathcal{I}$
$l \in \mathbb{R}$	Cable length
$\boldsymbol{\theta} = [\theta_x,\ \theta_y]^\top \in \mathbb{R}^2$	Payload swing angle
$\boldsymbol{q} = \left[\boldsymbol{\xi}^\top, l, \boldsymbol{\theta}^\top\right]^\top \in \mathbb{R}^6$	Combination vector
$\boldsymbol{s} = [s_x, s_y, s_z]^\top \in \mathbb{R}^3$	Normalized image feature
$\boldsymbol{s}_d = [s_{dx}, s_{dy}, s_{dz}]^\top \in \mathbb{R}^3$	Desired image feature
$l_d \in \mathbb{R}$	Desired cable length
$R_d \in SO(3)$	Desired rotation matrix from $\mathcal{B}$ to $\mathcal{I}$
$\boldsymbol{\Omega}_d \in \mathbb{R}^3$	Desired angular velocity of quadrotor
$f \in \mathbb{R}$	Applied thrust generated by quadrotor
$f_l \in \mathbb{R}$	Cable length adjusting force
$\boldsymbol{\tau} = [\tau_1, \tau_2, \tau_3]^\top \in \mathbb{R}^3$	Torque generated by quadrotor
$M_c(l, \boldsymbol{\theta}) \in \mathbb{R}^{6\times6}$	Inertia matrix
$V_c(l, \boldsymbol{\theta}, \dot{l}, \dot{\boldsymbol{\theta}}) \in \mathbb{R}^{6\times6}$	Centripetal-Coriolis matrix
$\boldsymbol{G}(l, \boldsymbol{\theta}) \in \mathbb{R}^6$	Gravity vector
$\boldsymbol{u} = [fR\boldsymbol{e}_3, f_l, 0, 0]^\top \in \mathbb{R}^6$	Outer loop control input vector

Assumption 2: The cable is massless, which is connected to the quadrotor's center of mass.

B. Image Features and Kinematics

For an arbitrary static point A, let $^\mathcal{C}\boldsymbol{A} = \left[{}^\mathcal{C}x, {}^\mathcal{C}y, {}^\mathcal{C}z\right]^\top$, $^\mathcal{V}\boldsymbol{A} = \left[{}^\mathcal{V}x, {}^\mathcal{V}y, {}^\mathcal{V}z\right]^\top$, $^\mathcal{I}\boldsymbol{A} = \left[{}^\mathcal{I}x, {}^\mathcal{I}y, {}^\mathcal{I}z\right]^\top$ denote the three-dimensional Euclidean coordinates expressed in $\mathcal{C}$, $\mathcal{V}$, and $\mathcal{I}$, respectively. Since the origin of frame $\mathcal{C}$ is coincided with frame $\mathcal{V}$, the relationship between $^\mathcal{V}\boldsymbol{A}$ and $^\mathcal{C}\boldsymbol{A}$ can be expressed as:

$$^\mathcal{V}\boldsymbol{A} = {}_\mathcal{C}^\mathcal{V}R\,{}^\mathcal{C}\boldsymbol{A} = {}_\mathcal{C}^\mathcal{I}R\,{}^\mathcal{C}\boldsymbol{A} = R\,{}^\mathcal{C}\boldsymbol{A}$$
$$\Rightarrow {}^\mathcal{V}x = \boldsymbol{e}_1^\top R\,{}^\mathcal{C}\boldsymbol{A}, {}^\mathcal{V}y = \boldsymbol{e}_2^\top R\,{}^\mathcal{C}\boldsymbol{A}, {}^\mathcal{V}z = \boldsymbol{e}_3^\top R\,{}^\mathcal{C}\boldsymbol{A}, \quad (1)$$

where $\boldsymbol{e}_1 = [1, 0, 0]^\top, \boldsymbol{e}_2 = [0, 1, 0]^\top, \boldsymbol{e}_3 = [0, 0, 1]^\top$ are unit vectors. Further, the coordinates of the static point A in frame $\mathcal{V}$ can be calculated as $^\mathcal{V}\boldsymbol{A} = {}_\mathcal{V}^\mathcal{I}R^\top \left({}^\mathcal{I}\boldsymbol{A} - \boldsymbol{\xi}\right)$, whose time derivative is given by

$$^\mathcal{V}\dot{\boldsymbol{A}} = -\dot{\boldsymbol{\xi}} = -\boldsymbol{v}. \quad (2)$$

Based on the perspective projection equation, the normalized image coordinate is represented as $\bar{\boldsymbol{\mu}} = \frac{^\mathcal{C}\boldsymbol{A}}{^\mathcal{C}z} = \left[\frac{^\mathcal{C}x}{^\mathcal{C}z}, \frac{^\mathcal{C}y}{^\mathcal{C}z}, 1\right]^\top \in \mathbb{R}^3$, which can be calculated by $\bar{\boldsymbol{\mu}} = K^{-1}\boldsymbol{n}$, with $K \in \mathbb{R}^{3 \times 3}$ and $\boldsymbol{n} = [u, v, 1]^\top \in \mathbb{R}^3$ being the known camera intrinsic matrix and image pixel coordinates, respectively. The normalized image coordinates in the rotated image plane is defined as $^\mathcal{V}\bar{\boldsymbol{\mu}} = \frac{^\mathcal{V}\boldsymbol{A}}{^\mathcal{V}z} = \left[{}^\mathcal{V}\bar{x}, {}^\mathcal{V}\bar{y}, 1\right]^\top = \left[\frac{^\mathcal{V}x}{^\mathcal{V}z}, \frac{^\mathcal{V}y}{^\mathcal{V}z}, 1\right]^\top \in \mathbb{R}^3$. Furthermore, with the help of (1), the relationship between the

normalized image coordinates in the original image plane and those in the rotated virtual image plane is:

$$^\mathcal{V}\bar{\boldsymbol{\mu}} = \frac{^\mathcal{C}z}{^\mathcal{V}z}{}_\mathcal{C}^\mathcal{V}R\bar{\boldsymbol{\mu}} = \frac{^\mathcal{C}z}{^\mathcal{V}z}R\bar{\boldsymbol{\mu}} = \frac{^\mathcal{C}z}{\boldsymbol{e}_3^\top R^\mathcal{C}\boldsymbol{A}}R\bar{\boldsymbol{\mu}} = \frac{1}{\boldsymbol{e}_3^\top R\bar{\boldsymbol{\mu}}}R\bar{\boldsymbol{\mu}}. \quad (3)$$

Subsequently, on the basis of (2), taking the time derivative of $^\mathcal{V}\bar{\boldsymbol{\mu}}$ yields

$$\begin{bmatrix} ^\mathcal{V}\dot{\bar{x}} \\ ^\mathcal{V}\dot{\bar{y}} \end{bmatrix} = \frac{1}{^\mathcal{V}z}\begin{bmatrix} -1 & 0 & ^\mathcal{V}\bar{x} \\ 0 & -1 & ^\mathcal{V}\bar{y} \end{bmatrix}\boldsymbol{v}. \quad (4)$$

Since there are $N > 1$ points in the target plane, image moments are chosen as image features. Define $^\mathcal{V}\bar{x}_g = \frac{1}{N}\sum_{k=1}^{N}{}^\mathcal{V}\bar{x}_k$, $^\mathcal{V}\bar{y}_g = \frac{1}{N}\sum_{k=1}^{N}{}^\mathcal{V}\bar{y}_k \in \mathbb{R}$ as the two dimension barycenter moments, $k \in \mathbb{N}_{[1,N]}$. Taking the time derivative of $^\mathcal{V}\bar{x}_g$ and $^\mathcal{V}\bar{y}_g$, then substituting (4) into the resultant equation, one has

$$\begin{bmatrix} ^\mathcal{V}\dot{\bar{x}}_g \\ ^\mathcal{V}\dot{\bar{y}}_g \end{bmatrix} = \frac{1}{^\mathcal{V}z}\begin{bmatrix} -1 & 0 & ^\mathcal{V}\bar{x}_g \\ 0 & -1 & ^\mathcal{V}\bar{y}_g \end{bmatrix}\boldsymbol{v}. \quad (5)$$

In addition, define the $(i + j)$-order centered moments as $^\mathcal{V}\mu_{ij} = \sum_{k=1}^{N}\left({}^\mathcal{V}\bar{x}_k - {}^\mathcal{V}\bar{x}_g\right)^i\left({}^\mathcal{V}\bar{y}_k - {}^\mathcal{V}\bar{y}_g\right)^j$ with positive exponents $i, j \in \mathbb{N}_0$. The second-order centered moment is calculated as $\gamma = {}^\mathcal{V}\mu_{20} + {}^\mathcal{V}\mu_{02} \in \mathbb{R}$. Therefore, the normalized image feature $\boldsymbol{s}$ can be defined as

$$\boldsymbol{s} = [s_x, s_y, s_z]^\top = \left[{}^\mathcal{V}\bar{x}_g s_z, {}^\mathcal{V}\bar{y}_g s_z, \sqrt{\frac{\gamma^\star}{\gamma}} \right]^\top, \quad (6)$$

where $\gamma^\star$ is the value of γ when the quadrotor is at the desired height. Taking the time derivative of (6), together with (5), one can obtain the kinematics of the image moment as:

$$\dot{\boldsymbol{s}} = -\frac{1}{z^\star}\boldsymbol{v}, \quad (7)$$

where $z^\star$ is the depth value when the camera is at desired pose, and satisfies the relationship $z^\star\sqrt{\gamma^\star} = {}^\mathcal{V}z\sqrt{\gamma}$. Thus, it can be seen from (7) that the kinematics of the image feature is independent of the quadrotor's rotation motion.

C. System Dynamics Transformation

According to the Lagrange's modeling method, the dynamic model of the aerial transportation system with variable-length cable is represented similar to [30] as:

$$M_c(l, \boldsymbol{\theta})\ddot{\boldsymbol{q}} + V_c(l, \boldsymbol{\theta}, \dot{l}, \dot{\boldsymbol{\theta}})\dot{\boldsymbol{q}} + \boldsymbol{G}(l, \boldsymbol{\theta}) = \boldsymbol{u}, \quad (8)$$
$$\dot{R} = R\hat{\boldsymbol{\Omega}}, \quad (9)$$
$$J\dot{\boldsymbol{\Omega}} + \boldsymbol{\Omega} \times J\boldsymbol{\Omega} = \boldsymbol{\tau}. \quad (10)$$

It can be proven that the outer loop subsystem (8) satisfies the following important property without much difficulty:

Property 1: Matrices $V_c(l, \boldsymbol{\theta}, \dot{l}, \dot{\boldsymbol{\theta}})$ and $M_c(l, \boldsymbol{\theta})$ satisfy the skew-symmetric relationship: $\boldsymbol{\eta}^\top\left(\frac{1}{2}\dot{M}_c - V_c\right)\boldsymbol{\eta} = 0, \ \forall\ \boldsymbol{\eta} \in \mathbb{R}^6$.

Rearranging and taking the time derivative of the image moment kinematics (7), one can obtain that

$$\boldsymbol{v} = -z^\star\dot{\boldsymbol{s}}, \ \dot{\boldsymbol{v}} = -z^\star\ddot{\boldsymbol{s}} \Rightarrow \dot{\boldsymbol{\xi}} = -z^\star\dot{\boldsymbol{s}}, \ \ddot{\boldsymbol{\xi}} = -z^\star\ddot{\boldsymbol{s}}. \quad (11)$$

Subsequently, inserting (11) into (8), the dynamics on image feature, cable length, and payload swing angle can be established as:

$$\begin{aligned} &- (M + m)z^\star\ddot{s}_x + ml\ddot{S}_xC_y + 2ml\dot{\theta}_xC_xC_y - 2ml\dot{\theta}_yS_xS_y \\ &+ ml\left(\ddot{\theta}_xC_xC_y - \ddot{\theta}_yS_xS_y - \dot{\theta}_x^2S_xC_y - \dot{\theta}_y^2S_xC_y - 2\dot{\theta}_x\dot{\theta}_yC_xS_y\right) \\ &= fR_{13}, \quad (12) \end{aligned}$$

$$\begin{aligned} &- (M + m)z^\star\ddot{s}_y + ml\ddot{S}_y + 2ml\dot{\theta}_yC_y + ml\left(\ddot{\theta}_yC_y - \dot{\theta}_y^2S_y\right) \\ &= fR_{23}, \quad (13) \end{aligned}$$

$$\begin{aligned} &- (M + m)z^\star\ddot{s}_z + ml\ddot{C}_xC_y - 2ml\dot{\theta}_xS_xC_y - 2ml\dot{\theta}_yC_xS_y \\ &- ml\left(\ddot{\theta}_xS_xC_y + \ddot{\theta}_yC_xS_y + \dot{\theta}_x^2C_xC_y + \dot{\theta}_y^2C_xC_y - 2\dot{\theta}_x\dot{\theta}_yS_xS_y\right) \\ &- (M + m)g = fR_{33}, \quad (14) \end{aligned}$$

$$\begin{aligned} &- mz^\star\ddot{s}_xS_xC_y - mz^\star\ddot{s}_yS_y - mz^\star\ddot{s}_zC_xC_y + ml\ddot{l} - ml\dot{\theta}_x^2C_y^2 \\ &- ml\dot{\theta}_y^2 - mgC_xC_y = f_l, \quad (15) \end{aligned}$$

$$\begin{aligned} &- mlz^\star\ddot{s}_xC_xC_y + mlz^\star\ddot{s}_zS_xC_y + ml^2\ddot{\theta}_xC_y^2 + 2ml\dot{l}\dot{\theta}_xC_y^2 \\ &- 2ml^2\dot{\theta}_x\dot{\theta}_yC_yS_y + mglS_xC_y = 0, \quad (16) \end{aligned}$$

$$\begin{aligned} &mlz^\star\ddot{s}_xS_xS_y - mlz^\star\ddot{s}_yC_y + mlz^\star\ddot{s}_zC_xS_y + ml^2\ddot{\theta}_y \\ &+ 2ml\dot{l}\dot{\theta}_y + ml^2\dot{\theta}_x^2C_yS_y + mglC_xS_y = 0, \quad (17) \end{aligned}$$

where $R\boldsymbol{e}_3 = [R_{13}, R_{23}, R_{33}]^\top$ represents the last column of rotation matrix R. Define vector $\boldsymbol{q}_s = \left[\boldsymbol{v}^\top, \dot{l}, \dot{\boldsymbol{\theta}}^\top\right]^\top = \left[-z^\star\dot{\boldsymbol{s}}^\top, \dot{l}, \dot{\boldsymbol{\theta}}^\top\right]^\top \in \mathbb{R}^6$. Thus, model (12)–(17) can be summarized as

$$M_c(l, \boldsymbol{\theta})\dot{\boldsymbol{q}}_s + V_c(l, \boldsymbol{\theta}, \dot{l}, \dot{\boldsymbol{\theta}})\boldsymbol{q}_s + \boldsymbol{G}(l, \boldsymbol{\theta}) = \boldsymbol{u}.$$

III. CONTROLLER DESIGN AND STABILITY ANALYSIS

In this section, an image-based visual servoing anti-swing control scheme is designed for the aerial transportation system with variable-length cable.

A. Control Objective

For the convenience of subsequent controller development and analysis, define the image feature error as $\boldsymbol{e}_s(t) = [e_{sx}, e_{sy}, e_{sz}]^\top = \boldsymbol{s} - \boldsymbol{s}_d$, and the cable length error as $e_l(t) = l - l_d$. The quadrotor's attitude and angular velocity tracking errors are defined as $\boldsymbol{e}_R = \frac{1}{2}\left(R_d^\top R - R^\top R_d\right)^\vee$, $\boldsymbol{e}_\Omega = \boldsymbol{\Omega} - R^\top R_d\boldsymbol{\Omega}_d$ [31]. The control objective of this paper is to design the applied force $\boldsymbol{u}$ and torque $\boldsymbol{\tau}$, so as to regulate the image feature to the desired image feature $\boldsymbol{s}_d$, adjust the cable length to the desired one l_d, and suppress the payload swing angle $\boldsymbol{\theta}$, in the following sense:

$$\boldsymbol{e}_s \rightarrow \boldsymbol{0}_{3\times1}, e_l \rightarrow 0, \boldsymbol{\theta} \rightarrow \boldsymbol{0}_{2\times1}, \boldsymbol{e}_R \rightarrow \boldsymbol{0}_{3\times1}, \boldsymbol{e}_\Omega \rightarrow \boldsymbol{0}_{3\times1}.$$

Fig. 2 shows the block diagram of the proposed method.

B. Controller Design

The energy function of the outer loop subsystem is given as

$$E = \frac{1}{2}\boldsymbol{q}_s^\top M_c\boldsymbol{q}_s + mgl\left(1 - C_xC_y\right). \quad (18)$$
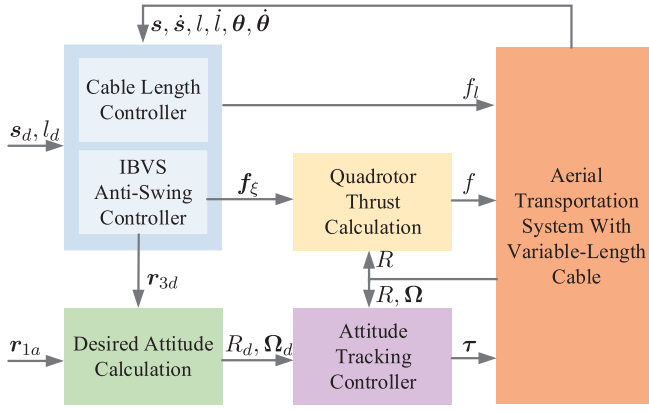
Fig. 2. Block diagram of the proposed control algorithm.

Invoking *Property 1* and taking the time derivative of (18) leads to

$$\dot{E} = \boldsymbol{q}_s^\top \left(M_c \dot{\boldsymbol{q}}_s + \frac{1}{2} \dot{M}_c \boldsymbol{q}_s \right) + mgl\left(\dot{\theta}_x S_x C_y + \dot{\theta}_y C_x S_y \right)$$
$$+ mg\dot{l}\left(1 - C_x C_y \right)$$
$$= \boldsymbol{\zeta}^\top \left(\left[f R \boldsymbol{e}_3^\top, f_l \right]^\top + \left[0, 0, (M+m)g, mg \right]^\top \right)$$
$$= \boldsymbol{\zeta}^\top \left(\left[\boldsymbol{f}_\xi^\top + \boldsymbol{f}_\Delta^\top, f_l \right]^\top + \left[0, 0, (M+m)g, mg \right]^\top \right), \quad (19)$$

where $\boldsymbol{\zeta} \in \mathbb{R}^4$ is defined as $\boldsymbol{\zeta} = [-z^\star \dot{\boldsymbol{s}}^\top, \dot{l}]^\top$, the virtual control input $\boldsymbol{f}_\xi = [f_x, f_y, f_z]^\top$ and the auxiliary vector $\boldsymbol{f}_\Delta$ are defined as $\boldsymbol{f}_\xi = \left(f/(\boldsymbol{e}_3^\top R_d^\top R \boldsymbol{e}_3) \right) R_d \boldsymbol{e}_3$, $\boldsymbol{f}_\Delta = \left(f/(\boldsymbol{e}_3^\top R_d^\top R \boldsymbol{e}_3) \right) \left[(\boldsymbol{e}_3^\top R_d^\top R \boldsymbol{e}_3) R \boldsymbol{e}_3 - R_d \boldsymbol{e}_3 \right]$. The hierarchical control theory can be adopted by viewing the actual attitude and the expected attitude as identical, which means that the coupling term $\boldsymbol{f}_\Delta$ can be temporarily neglected [30].

By substituting (11) into (19), $\dot{E}$ can be further written as:

$$\dot{E} = \boldsymbol{\zeta}^\top \left(\left[\boldsymbol{f}_\xi^\top, f_l \right]^\top + \left[0, 0, (M+m)g, mg \right]^\top \right)$$
$$= -z^\star \dot{\boldsymbol{s}}^\top \left(\boldsymbol{f}_\xi + (M+m)g\boldsymbol{e}_3 \right) + \dot{l}(f_l + mg)$$
$$= -z^\star \dot{\boldsymbol{e}}_s^\top \left(\boldsymbol{f}_\xi + (M+m)g\boldsymbol{e}_3 \right) + \dot{e}_l(f_l + mg). \quad (20)$$

To improve the payload swing suppression ability, based on the image feature error, a generalized virtual image feature signal $\boldsymbol{\delta} = [\delta_x, \delta_y, \delta_z]^\top \in \mathbb{R}^3$ is constructed as:

$$\boldsymbol{\delta} = -z^\star \boldsymbol{e}_s - \lambda \boldsymbol{\beta}$$
$$= -z^\star \boldsymbol{e}_s - \lambda \left[l S_x C_y, l S_y, (l C_x C_y - l_d) \right]^\top, \quad (21)$$

where $\lambda \in \mathbb{R}_+$ is a positive constant. Taking the time derivative of the composite signal (21), one has

$$\dot{\boldsymbol{\delta}} = -z^\star \dot{\boldsymbol{e}}_s - \lambda \begin{bmatrix} \dot{l} S_x C_y + l \dot{\theta}_x C_x C_y - l \dot{\theta}_y S_x S_y \\ \dot{l} S_y + l \dot{\theta}_y C_y \\ \dot{l} C_x C_y - l \dot{\theta}_x S_x C_y - l \dot{\theta}_y C_x S_y \end{bmatrix}. \quad (22)$$

Utilizing the composite position signal (21), a nonnegative function E_n can be constructed, whose time derivative is given as:

$$\dot{E}_n = \dot{\boldsymbol{\delta}}^\top \left(\boldsymbol{f}_\xi + (M+m)g\boldsymbol{e}_3 \right) + \frac{\lambda M + (1+\lambda)m}{m} \dot{e}_l(f_l + mg)$$
$$= \dot{E} + \dot{E}_a. \quad (23)$$

Combining with the system dynamic model (12)–(14), the expression of $\dot{E}_a$ can be further written as:

$$\dot{E}_a = -\lambda \dot{\boldsymbol{\beta}}^\top \left(\boldsymbol{f}_\xi + (M+m)g\boldsymbol{e}_3 \right) + \frac{\lambda(M+m)}{m} \dot{e}_l(f_l + mg)$$
$$= -(M+m)\lambda \dot{l}\left(-z^* \ddot{s}_x S_x C_y - z^* \ddot{s}_y S_y - z^* \ddot{s}_z C_x C_y \right)$$
$$- (M+m)\lambda l \dot{\theta}_x \left(-z^* \ddot{s}_x C_x C_y + z^* \ddot{s}_z S_x C_y \right)$$
$$- (M+m)\lambda l \dot{\theta}_y \left(z^* \ddot{s}_x S_x S_y - z^* \ddot{s}_y C_y + z^* \ddot{s}_z C_x S_y \right)$$
$$- \lambda \left(\dot{l} S_x C_y + l \dot{\theta}_x C_x C_y - l \dot{\theta}_y S_x S_y \right) \frac{\mathrm{d}}{\mathrm{d}t} \left[m \left(\dot{l} S_x C_y \right. \right.$$
$$\left. \left. + l \dot{\theta}_x C_x C_y - l \dot{\theta}_y S_x S_y \right) \right] - \lambda \left(\dot{l} S_y + l \dot{\theta}_y C_y \right) \frac{\mathrm{d}}{\mathrm{d}t} \left[m \left(\dot{l} S_y \right. \right.$$
$$\left. \left. + l \dot{\theta}_y C_y \right) \right] - \lambda \left(\dot{l} C_x C_y - l \dot{\theta}_x S_x C_y - l \dot{\theta}_y C_x S_y \right)$$
$$\times \frac{\mathrm{d}}{\mathrm{d}t} \left[m \left(\dot{l} C_x C_y - l \dot{\theta}_x S_x C_y - l \dot{\theta}_y C_x S_y \right) \right]$$
$$+ \frac{\lambda(M+m)}{m} \dot{l}(f_l + mg). \quad (24)$$

Then, substituting (15)–(17) into (24) yields

$$\dot{E}_a = -\lambda \left(\dot{l} S_x C_y + l \dot{\theta}_x C_x C_y - l \dot{\theta}_y S_x S_y \right) \frac{\mathrm{d}}{\mathrm{d}t} \left[m \left(\dot{l} S_x C_y \right. \right.$$
$$\left. \left. + l \dot{\theta}_x C_x C_y - l \dot{\theta}_y S_x S_y \right) \right] - \lambda \left(\dot{l} S_y + l \dot{\theta}_y C_y \right) \frac{\mathrm{d}}{\mathrm{d}t} \left[m \left(\dot{l} S_y \right. \right.$$
$$\left. \left. + l \dot{\theta}_y C_y \right) \right] - \lambda \left(\dot{l} C_x C_y - l \dot{\theta}_x S_x C_y - l \dot{\theta}_y C_x S_y \right)$$
$$\times \frac{\mathrm{d}}{\mathrm{d}t} \left[m \left(\dot{l} C_x C_y - l \dot{\theta}_x S_x C_y - l \dot{\theta}_y C_x S_y \right) \right] + \lambda(M+m)\ddot{l}\dot{l}$$
$$+ \lambda(M+m) \left(\dot{l} l \dot{\theta}_x^2 C_y^2 + l^2 \ddot{\theta}_x \dot{\theta}_x C_y^2 - l \dot{\theta}_x^2 \dot{\theta}_y C_y S_y \right)$$
$$+ \lambda(M+m) \left(l^2 \dot{\theta}_y \ddot{\theta}_y + \dot{l} l \dot{\theta}_y^2 \right) + \lambda(M+m)g \left(\dot{l} - \dot{l} C_x C_y \right.$$
$$\left. + l \dot{\theta}_x S_x C_y + l \dot{\theta}_y C_x S_y \right)$$
$$= -\frac{1}{2}\lambda m \frac{\mathrm{d}}{\mathrm{d}t} \left[\left(\dot{l} S_x C_y + l \dot{\theta}_x C_x C_y - l \dot{\theta}_y S_x S_y \right)^2 \right]$$
$$- \frac{1}{2}\lambda m \frac{\mathrm{d}}{\mathrm{d}t} \left[\left(\dot{l} S_y + l \dot{\theta}_y C_y \right)^2 \right] - \frac{1}{2}\lambda m \frac{\mathrm{d}}{\mathrm{d}t} \left[\left(\dot{l} C_x C_y \right. \right.$$
$$\left. \left. - l \dot{\theta}_x S_x C_y - l \dot{\theta}_y C_x S_y \right)^2 \right] + \frac{1}{2}\lambda(M+m) \frac{\mathrm{d}}{\mathrm{d}t} \left[\dot{l}^2 \right.$$
$$\left. + l^2 \dot{\theta}_x^2 C_y^2 + l^2 \dot{\theta}_y^2 + gl(1 - C_x C_y) \right]. \quad (25)$$

Subsequently, integrating (25) with time, E_a can be chosen as:

$$E_a = \frac{1}{2}\lambda M \left(\dot{l}^2 + l^2 \dot{\theta}_x^2 C_y^2 + l^2 \dot{\theta}_y^2 \right) + \lambda(M+m)gl\left(1 - C_x C_y \right), \quad (26)$$

which is positive obviously. Furthermore, construct the following positive definite function as:

$$V = E_n + \boldsymbol{k}_{ps} \mathrm{LnCosh}(\boldsymbol{\delta})$$
$$+ k_{pl} \frac{\lambda M + (1+\lambda)m}{m} \ln \cosh(e_l), \quad (27)$$

where $\boldsymbol{k}_{ps} = \left[k_{px}, k_{py}, k_{pz} \right]^\top \in \mathbb{R}_+^3$ is a positive definite vector, $k_{pl} \in \mathbb{R}_+$ is a positive control gain. Taking the time derivative of (27) yields

$$\dot{V} = \dot{E}_n + \dot{\boldsymbol{\delta}}^\top K_{ps} \mathrm{Tanh}(\boldsymbol{\delta}) + k_{pl} \dot{e}_l \frac{\lambda M + (1+\lambda)m}{m} \tanh(e_l)$$
$$= \dot{\boldsymbol{\delta}}^\top \left(\boldsymbol{f}_\xi + (M+m)g\boldsymbol{e}_3 + K_{ps} \mathrm{Tanh}(\boldsymbol{\delta}) \right)$$
$$+ \frac{\lambda M + (1+\lambda)m}{m} \dot{e}_l \left(f_l + mg + k_{pl} \tanh(e_l) \right), \quad (28)$$

where $K_{ps} = \text{diag}(\boldsymbol{k}_{ps}) \in \mathbb{R}_+^{3\times3}$. To avoid excessive control input caused by large state errors, the saturation function is introduced into the controller. Hence, based on the form of $\dot{V}$, the following control scheme can be constructed as:

$$\boldsymbol{f}_\xi = -K_{ps}\text{Tanh}(\boldsymbol{\delta}) - K_{ds}\text{Tanh}(\dot{\boldsymbol{\delta}}) - (M+m)g\boldsymbol{e}_3,$$
$$f_l = -k_{pl}\tanh(e_l) - k_{dl}\tanh(\dot{e}_l) - mg, \qquad (29)$$

where $K_{ds} = \text{diag}([k_{dx}, k_{dy}, k_{dz}]) \in \mathbb{R}_+^{3\times3}$ is a positive definite diagonal matrix, $k_{dl} \in \mathbb{R}_+$ is a positive control gain.

Further, according to the relation $\boldsymbol{f}_\xi = (f/(\boldsymbol{e}_3^\top R_d^\top R\boldsymbol{e}_3))R_d\boldsymbol{e}_3$, it is obvious that $\boldsymbol{f}_\xi$ and $R_d\boldsymbol{e}_3$ have the same direction, thus, the desired unit direction vector $\boldsymbol{r}_{3d} = R_d\boldsymbol{e}_3 \in \mathbb{R}^3$ can be obtained by calculating $\boldsymbol{r}_{3d} = R_d\boldsymbol{e}_3 = \boldsymbol{f}_\xi/\|\boldsymbol{f}_\xi\|$. Then, $\boldsymbol{f}_\xi$ can be further arranged as $\boldsymbol{f}_\xi = \frac{f\|\boldsymbol{f}_\xi\|}{\boldsymbol{f}_\xi^\top R\boldsymbol{e}_3} \cdot \frac{\boldsymbol{f}_\xi}{\|\boldsymbol{f}_\xi\|} = \frac{f\cdot\boldsymbol{f}_\xi}{\boldsymbol{f}_\xi^\top R\boldsymbol{e}_3}$, which indicates that the scaler quadrotor thrust can be calculated by $f = \boldsymbol{f}_\xi^\top R\boldsymbol{e}_3$. Besides, on the basis of the obtained unit vector $\boldsymbol{r}_{3d}$, selecting an arbitrary vector $\boldsymbol{r}_{1a}(t) \in \mathbb{R}^3$ not parallel to $\boldsymbol{r}_{3d}$, the desired attitude can be derived as $R_d(t) = [\boldsymbol{r}_{2d} \times \boldsymbol{r}_{3d}; \boldsymbol{r}_{2d}; \boldsymbol{r}_{3d}]$, where $\boldsymbol{r}_{2d} = \frac{\boldsymbol{r}_{3d}\times\boldsymbol{r}_{1a}}{\|\boldsymbol{r}_{3d}\times\boldsymbol{r}_{1a}\|}$ represents the second row of the desired rotation matrix. Subsequently, the desired angular velocity and its time derivative can be calculated as $\boldsymbol{\Omega}_d = (R_d^\top \dot{R}_d)^\vee$, and $\dot{\boldsymbol{\Omega}}_d = (R_d^\top \ddot{R}_d - \hat{\Omega}_d^2)^\vee$ [31], [32], [33], [34].

Remark 1: For the desired attitude tracking problem, adopt the following control approach [31]:

$$\boldsymbol{\tau} = -K_R\boldsymbol{e}_R - K_\Omega\boldsymbol{e}_\Omega + \hat{\boldsymbol{\Omega}}J\boldsymbol{\Omega}$$
$$- J(\hat{\boldsymbol{\Omega}}R^\top R_d\boldsymbol{\Omega}_d - R^\top R_d\dot{\boldsymbol{\Omega}}_d), \qquad (30)$$

wherein $K_R, K_\Omega \in \mathbb{R}_+^{3\times3}$ are positive definite diagonal matrices. Explicitly, the control law (30) can drive the attitude and angular velocity tracking errors, i.e., $\boldsymbol{e}_R(t)$, $\boldsymbol{e}_\Omega(t)$, to zero exponentially.

C. Stability Analysis

Theorem 1: Based on the developed control scheme (29), the equilibrium point is asymptotically stable. The image feature can be driven to the desired one, the cable is adjusted to the desired length, and the payload swing is eliminated effectively, i.e.,

$$\lim_{t\to\infty} \boldsymbol{s} = \boldsymbol{s}_d, \lim_{t\to\infty} l = l_d, \lim_{t\to\infty} \boldsymbol{\theta} = \boldsymbol{0}_{2\times1}.$$

Proof: Selecting (28) as the Lyapunov function candidate. Substituting (29) into the time derivative of (28) yields

$$\dot{V} = -\dot{\boldsymbol{\delta}}^\top K_{ds}\text{Tanh}(\dot{\boldsymbol{\delta}}) - k_{dl}\frac{\lambda M + (1+\lambda)m}{m}\dot{e}_l\tanh(\dot{e}_l)$$
$$\leq 0. \qquad (31)$$

Therefore, by concluding (27), (29) and (31), the following result can be derived that

$$e_{sx}, e_{sy}, e_{sz}, e_l, \dot{s}_x, \dot{s}_y, \dot{s}_z, \dot{l}, \dot{\theta}_x, \dot{\theta}_y, \boldsymbol{f}_\xi, f_l \in \mathcal{L}_\infty. \qquad (32)$$

Subsequently, LaSalle's Invariance Theorem [35] will be employed to accomplish the proof. Define the set Π as

$$\Pi = \{(\boldsymbol{e}_s, e_l, \boldsymbol{\theta}, \dot{\boldsymbol{e}}_s, \dot{e}_l, \dot{\boldsymbol{\theta}}) | \dot{V}(t) = 0\},$$

and let Λ be the largest invariant set in Π. Thus, under (31), it is obviously that in Λ the following conclusion holds:

$$\dot{\boldsymbol{\delta}} = \boldsymbol{0}_{3\times1}, \dot{e}_l = 0, \qquad (33)$$

which indicates that

$$-z^\star\dot{e}_{sx} - \lambda(\dot{l}S_xC_y + l\dot{\theta}_xC_xC_y - l\dot{\theta}_yS_xS_y) = 0, \qquad (34)$$
$$-z^\star\dot{e}_{sy} - \lambda(\dot{l}S_y + l\dot{\theta}_yC_y) = 0, \qquad (35)$$
$$-z^\star\dot{e}_{sz} - \lambda(\dot{l}C_xC_y - l\dot{\theta}_xS_xC_y - l\dot{\theta}_yC_xS_y) = 0. \qquad (36)$$

Whereafter, integrate and derivate the result in (33) with respect to time, respectively, one can obtain that

$$\boldsymbol{\delta} = \boldsymbol{\varpi}_s, e_l = \varpi_l, \qquad (37)$$
$$\ddot{\boldsymbol{\delta}} = -z^\star\ddot{\boldsymbol{e}}_s - \lambda\ddot{\boldsymbol{\beta}} = \boldsymbol{0}_{3\times1}, \ddot{e}_l = 0, \qquad (38)$$

where $\boldsymbol{\varpi}_s = [\varpi_{sx}, \varpi_{sy}, \varpi_{sz}]^\top$ represents an undetermined constant vector and ϖ_l denotes an undetermined constant. Then, it follows from (38) that

$$-z^\star\ddot{e}_{sx} - \lambda[\ddot{l}S_xC_y + 2\dot{l}\dot{\theta}_xC_xC_y - 2\dot{l}\dot{\theta}_yS_xS_y + l(\ddot{\theta}_xC_xC_y$$
$$-\ddot{\theta}_yS_xS_y - \dot{\theta}_x^2S_xC_y - \dot{\theta}_y^2S_xC_y - 2\dot{\theta}_x\dot{\theta}_yC_xS_y)] = 0, \qquad (39)$$
$$-z^\star\ddot{e}_{sy} - \lambda[\ddot{l}S_y + 2\dot{l}\dot{\theta}_yC_y + l(\ddot{\theta}_yC_y - \dot{\theta}_y^2S_y)] = 0, \qquad (40)$$
$$-z^\star\ddot{e}_{sz} - \lambda[\ddot{l}C_xC_y - 2\dot{l}\dot{\theta}_xS_xC_y - 2\dot{l}\dot{\theta}_yC_xS_y - l(\ddot{\theta}_xS_xC_y$$
$$+\ddot{\theta}_yC_xS_y + \dot{\theta}_x^2C_xC_y + \dot{\theta}_y^2C_xC_y - 2\dot{\theta}_x\dot{\theta}_yS_xS_y)] = 0. \qquad (41)$$

Substituting (33) and (37) into (29), one can obtain that

$$\boldsymbol{f}_\xi = -K_{ps}\text{Tanh}(\boldsymbol{\varpi}_s) - (M+m)g\boldsymbol{e}_3, \qquad (42)$$
$$f_l = -k_{pl}\tanh(\varpi_l) + mg. \qquad (43)$$

Subsequently, inserting (42) into (12)–(14), and comparing the result with (39)–(41) yields

$$\frac{k_{px}\tanh(\varpi_{sx}) + (M+m)z^*\ddot{s}_x}{m} = \frac{-z^*\ddot{e}_{sx}}{\lambda}, \qquad (44)$$
$$\frac{k_{py}\tanh(\varpi_{sy}) + (M+m)z^*\ddot{s}_y}{m} = \frac{-z^*\ddot{e}_{sy}}{\lambda}, \qquad (45)$$
$$\frac{k_{pz}\tanh(\varpi_{sz}) + (M+m)z^*\ddot{s}_z}{m} = \frac{-z^*\ddot{e}_{sz}}{\lambda}. \qquad (46)$$

Since $\ddot{\boldsymbol{s}} = \ddot{\boldsymbol{e}}_s$, (44)–(46) can be further derived as

$$-z^\star\ddot{e}_{sx} = -\frac{\lambda k_{px}\tanh(\varpi_{sx})}{\lambda(M+m)+m}, \qquad (47)$$
$$-z^\star\ddot{e}_{sy} = -\frac{\lambda k_{py}\tanh(\varpi_{sy})}{\lambda(M+m)+m}, \qquad (48)$$
$$-z^\star\ddot{e}_{sz} = -\frac{\lambda k_{pz}\tanh(\varpi_{sz})}{\lambda(M+m)+m}. \qquad (49)$$

Assuming $\varpi_{sx} \neq 0, \varpi_{sy} \neq 0, \varpi_{sz} \neq 0$, one can conclude that $\dot{e}_{sx} \to \infty, \dot{e}_{sy} \to \infty, \dot{e}_{sz} \to \infty$ as $t \to \infty$, which conflicts with the conclusion $\dot{e}_{sx}, \dot{e}_{sy}, \dot{e}_{sz} \in \mathcal{L}_\infty$. Therefore, the assumption $\varpi_{sx} \neq 0, \varpi_{sy} \neq 0, \varpi_{sz} \neq 0$

does not hold, thus from (37) and (47)–(49), one can obtain that

$$\boldsymbol{\varpi}_s = \mathbf{0}_{3\times 1}, \ddot{e}_{sx} = 0, \ddot{e}_{sy} = 0, \ddot{e}_{sz} = 0$$
$$\Rightarrow \boldsymbol{\delta} = \mathbf{0}_{3\times 1}, \dot{e}_{sx} = \varepsilon_{sx}, \dot{e}_{sy} = \varepsilon_{sy}, \dot{e}_{sz} = \varepsilon_{sz}, \quad (50)$$

where $\varepsilon_{sx}, \varepsilon_{sy}, \varepsilon_{sz}$ represent undetermined constants. In an analogous method, assuming $\varepsilon_{sx} \neq 0, \varepsilon_{sy} \neq 0, \varepsilon_{sz} \neq 0$, one achieves that $e_{sx} \to \infty, e_{sy} \to \infty, e_{sz} \to \infty$ as $t \to \infty$, which is inconsistent with the result $e_{sx}, e_{sy}, e_{sz} \in \mathcal{L}_\infty$. Thus, one has

$$\varepsilon_{sx} = 0, \varepsilon_{sy} = 0, \varepsilon_{sz} = 0 \Rightarrow \dot{e}_{sx} = 0, \dot{e}_{sy} = 0, \dot{e}_{sz} = 0. \quad (51)$$

Subsequently, according to *Assumption 1* and the results in (34)–(36) and (51), it follows that

$$\dot{\theta}_x C_x C_y - \dot{\theta}_y S_x S_y = 0, \dot{\theta}_y C_y = 0, \dot{\theta}_x S_x C_y + \dot{\theta}_y C_x S_y = 0,$$

which means that

$$\dot{\theta}_x = 0, \dot{\theta}_y = 0 \Rightarrow \ddot{\theta}_x = 0, \ddot{\theta}_y = 0. \quad (52)$$

Substituting (33) and (50)–(52) into (16) and (17) achieves that

$$mgl S_x C_y = 0, mgl C_x S_y = 0 \Rightarrow \theta_x = 0, \theta_y = 0. \quad (53)$$

Furthermore, substituting (43), (52) and (53) into (15), one can obtain that

$$-k_{pl} \tanh(\varpi_l) = 0 \Rightarrow \varpi_l = 0 \Rightarrow e_l = 0 \Rightarrow l = l_d. \quad (54)$$

Then, substituting (53) and (54) into the result $\boldsymbol{\delta} = \mathbf{0}_{3\times 1}$, one has

$$\boldsymbol{e}_s = \mathbf{0}_{3\times 1} \Rightarrow \boldsymbol{s} = \boldsymbol{s}_d. \quad (55)$$

In summary, based on (33), (51)–(55), one can conclude that the largest invarient set Λ only contains the equilibrium point. Thus, it shows that *Theorem 1* holds. ∎

Theorem 2: The proposed control law (29) and (30) can regulate the image moment to the desired one, adjust the cable to the desired state, and suppress the payload swing, implying the following result:

$$\lim_{t\to\infty} \left[\boldsymbol{s}^\top, \dot{\boldsymbol{s}}^\top, l, \dot{l}, \boldsymbol{\theta}^\top, \dot{\boldsymbol{\theta}}^\top, \boldsymbol{e}_R^\top, \boldsymbol{e}_\Omega^\top\right]^\top$$
$$= \left[\boldsymbol{s}_d^\top, \mathbf{0}_{3\times 1}^\top, l_d, 0, \mathbf{0}_{2\times 1}^\top, \mathbf{0}_{2\times 1}^\top, \mathbf{0}_{3\times 1}^\top, \mathbf{0}_{3\times 1}^\top\right]^\top.$$

Proof: The stability analysis of the overall closed-loop system with the consideration of the coupling term $\boldsymbol{f}_\Delta$ is taken into account here. Define the generalized vector as $\boldsymbol{e} = \left[-z^* \boldsymbol{e}_s^\top, e_l, \boldsymbol{\theta}^\top, -z^* \dot{\boldsymbol{e}}_s^\top, \dot{e}_l, \dot{\boldsymbol{\theta}}^\top\right]^\top \in \mathbb{R}^{12}$. Inserting $R_d \boldsymbol{e}_3 = \frac{\boldsymbol{f}_\xi}{\|\boldsymbol{f}_\xi\|}$ and $f = \boldsymbol{f}_\xi^\top R \boldsymbol{e}_3$ into $\boldsymbol{f}_\Delta$, and according to reference [31], one can obtain

$$\|\boldsymbol{f}_\Delta\| = \|\boldsymbol{f}_\xi\| \|\left(\boldsymbol{e}_3^\top R_d^\top R \boldsymbol{e}_3\right) R \boldsymbol{e}_3 - R_d \boldsymbol{e}_3\|$$
$$\leq \|\boldsymbol{f}_\xi\| \|\boldsymbol{e}_R\|. \quad (56)$$

Let $\bar{l}$ denote the upper bound of the cable length, and from (21) and (22), the following conditions hold as:

$$\|\boldsymbol{\beta}\| = \sqrt{l^2 - 2l l_d C_x C_y + l_d^2} \leq e_l + 2l_d,$$

$$\|\dot{\boldsymbol{\beta}}\| = \sqrt{\dot{l}^2 + l^2 \dot{\theta}_x^2 C_y^2 + l^2 \dot{\theta}_y^2} \leq \max(1, \bar{l})\sqrt{\|\dot{e}_l\|^2 + \|\dot{\boldsymbol{\theta}}\|^2}.$$

Thus, according to the fact that $|\tanh(\cdot)| < |\cdot|$, the virtual control input $\boldsymbol{f}_\xi$ satisfies that

$$\|\boldsymbol{f}_\xi\| \leq \|K_{ps}\boldsymbol{\delta}\| + \|K_{ds}\dot{\boldsymbol{\delta}}\| + (M+m)g$$
$$\leq 2\max(\lambda_{ps}, \lambda_{ds}) \cdot \max(1, \lambda, \lambda\bar{l})\|\boldsymbol{e}\|$$
$$\quad + 2\lambda \max(\lambda_{ps}, \lambda_{ds})l_d + (M+m)g. \quad (57)$$

By selecting

$$\rho = 4\max(\lambda_{ps}, \lambda_{ds}) \cdot \max(1, \lambda, \lambda\bar{l}),$$
$$\varrho = \frac{(M+m)g + 2\lambda\max(\lambda_{ps}, \lambda_{ds})l_d}{2\max(\lambda_{ps}, \lambda_{ds}) \cdot \max(1, \lambda, \lambda\bar{l})},$$

one knows that the virtual control input $\boldsymbol{f}_\xi$ presents the following property:

$$\|\boldsymbol{f}_\xi(\boldsymbol{e})\| \leq \begin{cases} \rho\|\boldsymbol{e}\|, & \text{for } \|\boldsymbol{e}\| \geq \varrho \\ \rho\varrho, & \text{for } \|\boldsymbol{e}\| < \varrho. \end{cases} \quad (58)$$

Then, substituting the result (58) into (56), the coupling term can be further deduced as:

$$\|\boldsymbol{f}_\Delta\| \leq \|\boldsymbol{f}_\xi\| \|\boldsymbol{e}_R\|$$
$$\leq \rho\|\boldsymbol{e}\|\|\boldsymbol{e}_R\|, \text{ for } \|\boldsymbol{e}\| \geq \varrho,$$

which means that the coupling term $\boldsymbol{f}_\Delta$ satisfies the growth restriction condition. Thus, as shown in [36] and [37], the stability of the overall system is proven. ∎

As the desired angular velocity $\boldsymbol{\Omega}_d$ and angular acceleration $\dot{\boldsymbol{\Omega}}_d$ exist in almost all geometric controllers [8], [31], [32], [33], [34], $\dot{R}_d$ and $\ddot{R}_d$ relevant to the time derivatives of the desired thrust force $\boldsymbol{f}_\xi$ are commonly needed, which can be obtained according to a complex derivation of the system dynamic model (12)–(17). To avoid the complicated derivations, [38] assumes that the flight control unit can achieve the desired angular rate nearly instantaneously and neglects the angular rate dynamics. For small deviations from the hover position, [39], [40] verify that the geometric controller remains stable in the absence of the last two terms in (30). Also, filtered numerical differentiation is a commonly used engineering method to avoid complex derivation, which is utilized in this paper and achieves satisfactory performance. In practical experiments, the processing methods of these high-order signals can be selected based on the computational capabilities of the onboard computing unit.

Remark 2: This paper mainly deals with the control objectives of image feature tracking, cable length adjusting and payload swing suppression for aerial transportation system with variable-length cable. When external disturbances exist, the dynamic model of the system becomes

$$M_c(l, \boldsymbol{\theta})\dot{\boldsymbol{q}}_s + V_c(l, \boldsymbol{\theta}, \dot{l}, \dot{\boldsymbol{\theta}})\boldsymbol{q}_s + G(l, \boldsymbol{\theta}) = \boldsymbol{u} + \boldsymbol{d}_f,$$
$$\dot{R} = R\hat{\boldsymbol{\Omega}},$$
$$J\dot{\boldsymbol{\Omega}} + \boldsymbol{\Omega} \times J\boldsymbol{\Omega} = \boldsymbol{\tau} + \boldsymbol{d}_\tau,$$

where $\boldsymbol{d}_f = [d_x, d_y, d_z, d_l, d_{\theta_x}, d_{\theta_y}] \in \mathbb{R}^6$ and $\boldsymbol{d}_\tau = [d_1, d_2, d_3] \in \mathbb{R}^3$ denote the disturbances on the translation

Fig. 3. Experimental platform.

(a) Image feature, cable length and payload swing angles.

(b) Control inputs.

(c) Paths of feature points.

Fig. 4. Results for *Basic Performance Test*.
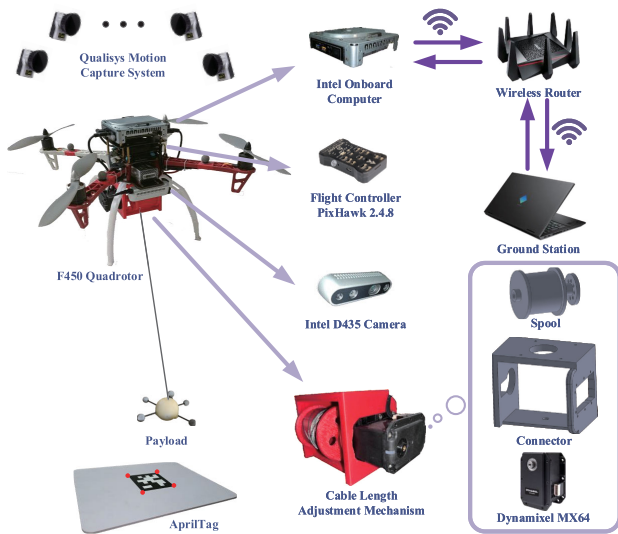
dynamic and rotation dynamic. Under the current control framework, it is difficult to analyze the robustness of the proposed control scheme (29) and (30) against external disturbances. Therefore, we will concentrate on designing more advanced control schemes to take care of disturbances for both the actuated part and the underactuated one in future efforts.

IV. EXPERIMENTAL IMPLEMENTATION AND RESULTS

To verify the validity of the designed image-based anti-swing controller, two groups of experiments are conducted in this section.

A. Experimental Platform

With the support of Robot Operating System (ROS), the experiments are conducted on the self-built experimental platform as shown in Fig. 3. The aerial transportation system is composed of an Intel onboard computer, a PixHawk flight controller, an Intel D435 camera, and a cable length adjustment mechanism. The onboard computer is logged in remotely from the ground station via the wireless router, which sends control instructions to the flight controller through MAVROS. The camera is utilized to detect the AprilTag with a sampling rate of 30Hz. It should be noted that we only use the information of four corner points of the AprilTag in red as marked in Fig. 3, while the physical distance is not employed in the IBVS controller. The cable length adjustment mechanism, which is utilized to stretch and shorten the cable length, consists of a Dynamixel MX-64 actuator, a 3-D-printed quadrotor-actuator connector and a 3-D-printed spool.

The physical parameters of the experimental platform are given as $M = 2.18$ kg, $m = 0.14$ kg, $g = 9.8$ m/s^2, $J = \text{diag}([0.0504, 0.0518, 0.0628])$ kg$\cdot$m^2. The desired second-order centered moment is chosen as $\gamma^* = 0.010$. The control gains are selected as: $K_{ps} = \text{diag}([5.5, 5.5, 7.0])$, $K_{ds} = \text{diag}([7.0, 7.0, 14.0])$, $k_{pl} = 4.0$, $k_{dl} = 6.0$, $\lambda = 0.23$, $K_R = \text{diag}([1.92, 1.92, 1.92])$, $K_\Omega = \text{diag}([0.3, 0.3, 0.3])$.
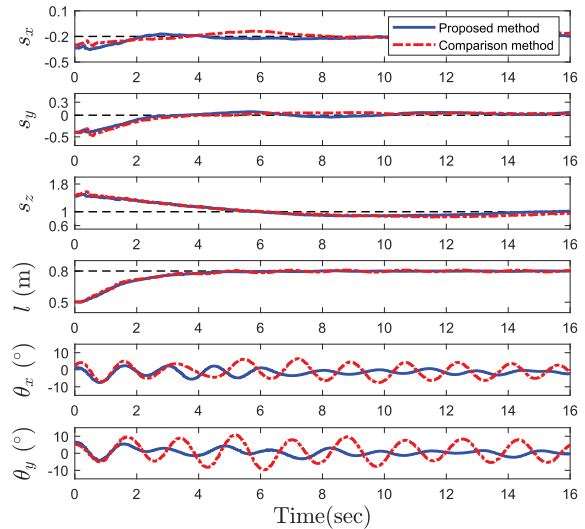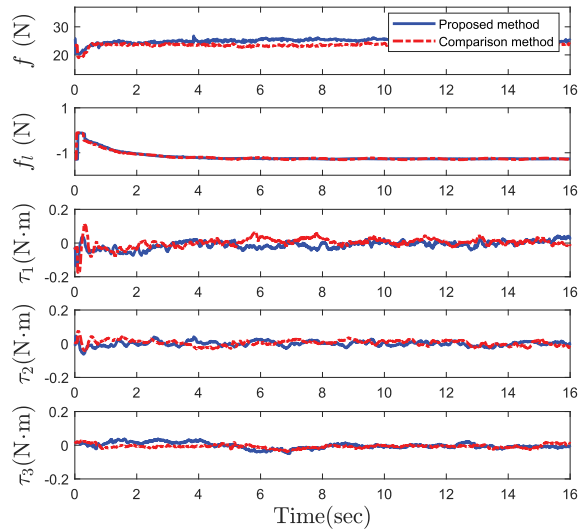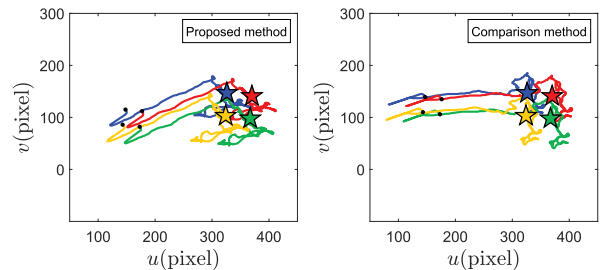
B. Basic Performance Test

To test the basic performance of the designed control scheme, a group of comparison experiment is implemented in this part. The comparison method does not contain payload swing angle information, which takes the following form as:

$$f_{\xi c} = -K_{ps}\text{Tanh}(\boldsymbol{e}_s) - K_{ds}\text{Tanh}(\dot{\boldsymbol{e}}_s) - (M+m)g\boldsymbol{e}_3,$$
$$f_{lc} = -k_{pl}\tanh(e_l) - k_{dl}\tanh(\dot{e}_l) - mg,$$

(a) Snapshot.   (b) Trajectories.
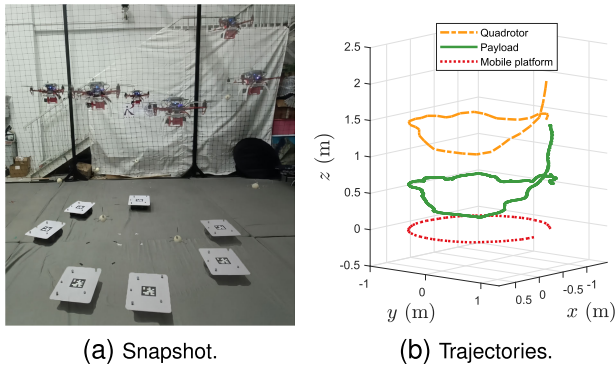
Fig. 5. Process of *Function Demonstration Test*.

whose control gains are selected the same as the proposed method. The initial image feature is $s(0) = [-0.2, -0.4, 1.5]^\top$, and the desired image feature is set as $s_d = [-0.1, 0.0, 1.0]^\top$. The initial cable length is $l(0) = 0.5$ m, and the final cable length is $l_d = 0.8$ m. Fig. 4 provides the experiment curves of the basic performance test. It is clear that both methods could drive the image feature to the desired one and adjust the cable to the target length. Fig. 4c displays the paths of four feature points in the pixel planes, where the black points denote the extracted feature points in the initial image and the pentagram ones are the reference points in the desired image, from which one knows that both method can drive the feature points to reach the reference points. Notably, as shown in Fig. 4a, with the help of the generalized virtual image feature signal, the proposed method exhibits better anti-swing performance, whose payload swing angles can be quickly suppressed, while the payload swing angles of the comparison method naturally decay after reaching the target image feature.

C. Function Demonstration Test

To further verify the effectiveness of the designed controller in practical applications, a functional demonstration test is conducted in this subsection. The AprilTag is placed on a mobile platform, whose trajectory is set as

$$x_v = [\sin(0.15t), \cos(0.15t), 0]^\top.$$

The initial and desired system states are set as: $s(0) = [-0.2, 0.0, 1.5]^\top$, $l(0) = 0.6$ m, $s_d = [-0.15, 0.0, 1.0]^\top$, $l_d = 0.85$ m. Notably, the trajectory of the mobile platform is priori unknown for the aerial transportation system. As the mobile platform moves, the image feature will change in the image plane. To track the target image feature, the aerial transportation system will move along with the mobile platform. The process of the experiment is presented in Fig. 5, where Fig. 5a shows the snapshot and Fig. 5b shows the trajectories in Cartesian space. The experiment curves are given in Fig. 6, from which one can see that the cable converges to the desired length, and the swing angles of the payload are kept within a small range during the tracking process. Besides, Fig. 6c shows that the four visual feature points always move around the target feature points, indicating the robustness of the proposed method.
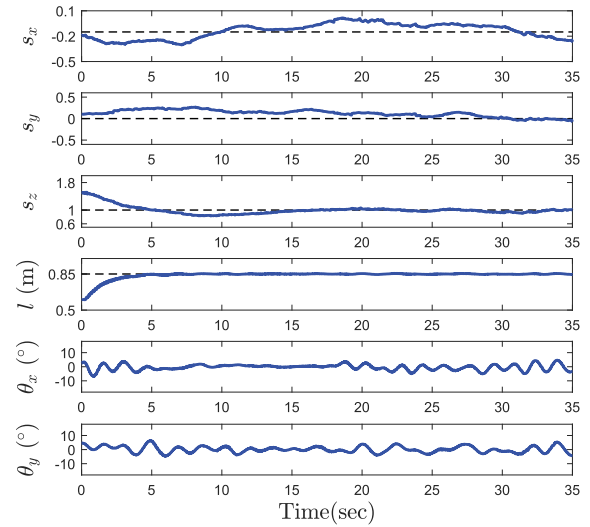
(a) Image feature, cable length and payload swing angles.
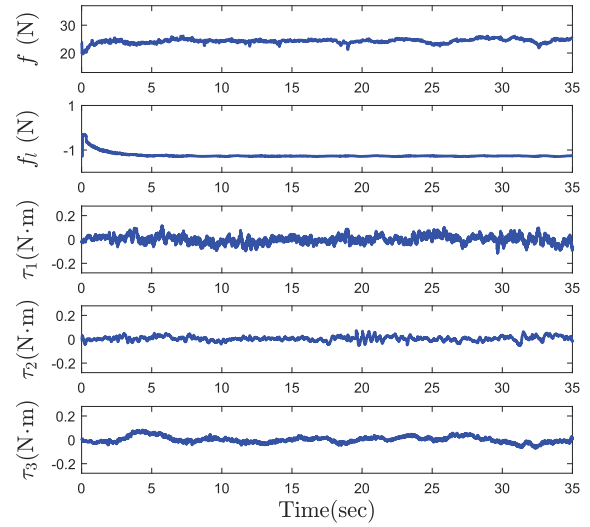
(b) Control inputs.
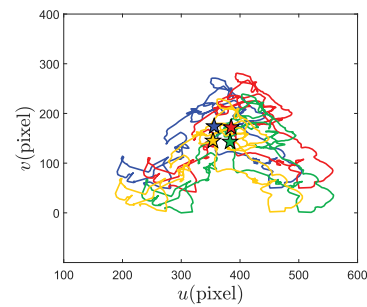
(c) Paths of feature points.

Fig. 6. Results for *Function Demonstration Test*.

V. CONCLUSION

This paper proposes an image-based visual servoing anti-swing control scheme for the aerial transportation system with variable-length cable. Specifically, the controller is designed based on a generalized virtual image feature signal, which greatly improves the anti-swing ability while ensuring accurate target tracking and cable length adjusting. Lyapunov techniques and LaSalle's Invariance Theorem are utilized to

guarantee the asymptotical stability of the overall closed-loop system. Two groups of experimental results are presented to demonstrate the excellent performance of the control law in target point tracking and payload swing suppressing. In the future, we will focus on the visibility of the mobile platform and algorithm design to constrain the payload within the boundaries of the mobile platform.

REFERENCES

[1] D. Lin, W. Chen, K. He, N. Jiao, Z. Wang, and L. Liu, "Position and orientation control of multisection magnetic soft microcatheters," *IEEE/ASME Trans. Mechatron.*, vol. 28, no. 2, pp. 907–918, Apr. 2023.

[2] J. M. Li, D. D. Molinaro, A. S. King, A. Mazumdar, and A. J. Young, "Design and validation of a cable-driven asymmetric back exosuit," *IEEE Trans. Robot.*, vol. 38, no. 3, pp. 1489–1502, Jun. 2022.

[3] W. Shang, H. Ren, Z. Yi, T. Xu, and X. Wu, "High precision PCB soldering with pin springback compensation by robotic micromanipulation," *IEEE/ASME Trans. Mechatronics*, vol. 28, no. 1, pp. 326–339, Feb. 2023.

[4] X. Wu, Y. Zhao, and K. Xu, "Nonlinear disturbance observer based sliding mode control for a benchmark system with uncertain disturbances," *ISA Trans.*, vol. 110, pp. 63–70, Apr. 2021.

[5] G. Chen et al., "Design and control of a novel bionic mantis shrimp robot," *IEEE/ASME Trans. Mechatronics*, vol. 28, no. 6, pp. 3376–3385, Dec. 2023.

[6] G. Rizzi, J. J. Chung, A. Gawel, L. Ott, M. Tognon, and R. Siegwart, "Robust sampling-based control of mobile manipulators for interaction with articulated objects," *IEEE Trans. Robot.*, vol. 39, no. 3, pp. 1929–1946, Jun. 2023.

[7] Y. Qian, D. Hu, Y. Chen, and Y. Fang, "Programming-based optimal learning sliding mode control for cooperative dual ship-mounted cranes against unmatched external disturbances," *IEEE Trans. Autom. Sci. Eng.*, vol. 20, no. 2, pp. 969–980, Apr. 2023.

[8] J. Zeng, P. Kotaru, and K. Sreenath, "Geometric control and differential flatness of a quadrotor UAV with load suspended from a pulley," in *Proc. Amer. Control Conf. (ACC)*, Jul. 2019, pp. 2420–2427.

[9] Z. Lv, Y. Wu, X.-M. Sun, and Q.-G. Wang, "Fixed-time control for a quadrotor with a cable-suspended load," *IEEE Trans. Intell. Transp. Syst.*, vol. 23, no. 11, pp. 21932–21943, Nov. 2022.

[10] B. Xian and S. Yang, "Robust tracking control of a quadrotor unmanned aerial vehicle-suspended payload system," *IEEE/ASME Trans. Mechatronics*, vol. 26, no. 5, pp. 2653–2663, Oct. 2021.

[11] G. Yu, D. Cabecinhas, R. Cunha, and C. Silvestre, "Aggressive maneuvers for a quadrotor-slung-load system through fast trajectory generation and tracking," *Auton. Robots*, vol. 46, pp. 499–513, Mar. 2022.

[12] J. Zeng, P. Kotaru, M. W. Mueller, and K. Sreenath, "Differential flatness based path planning with direct collocation on hybrid modes for a quadrotor with a cable-suspended payload," *IEEE Robot. Autom. Lett.*, vol. 5, no. 2, pp. 3074–3081, Apr. 2020.

[13] D. Hashemi and H. Heidari, "Trajectory planning of quadrotor UAV with maximum payload and minimum oscillation of suspended load using optimal control," *J. Intell. Robotic Syst.*, vol. 100, pp. 1369–1381, Dec. 2020.

[14] J. Lin, Y. Wang, Z. Miao, H. Zhong, and R. Fierro, "Low-complexity control for vision-based landing of quadrotor UAV on unknown moving platform," *IEEE Trans. Ind. Informat.*, vol. 18, no. 8, pp. 5348–5358, Aug. 2022.

[15] W. Zhao, H. Liu, F. L. Lewis, K. P. Valavanis, and X. Wang, "Robust visual servoing control for ground target tracking of quadrotors," *IEEE Trans. Control Syst. Technol.*, vol. 28, no. 5, pp. 1980–1987, Sep. 2020.

[16] Y. Liu, Z. Meng, Y. Zou, and M. Cao, "Visual object tracking and servoing control of a nano-scale quadrotor: System, algorithms, and experiments," *IEEE/CAA J. Autom. Sinica*, vol. 8, no. 2, pp. 344–360, Feb. 2021.

[17] A. Paris, B. T. Lopez, and J. P. How, "Dynamic landing of an autonomous quadrotor on a moving platform in turbulent wind conditions," in *Proc. IEEE Int. Conf. Robot. Autom. (ICRA)*, May 2020, pp. 9577–9583.

[18] J. Lin, Y. Wang, Z. Miao, S. Fan, and H. Wang, "Robust observer-based visual servo control for quadrotors tracking unknown moving targets," *IEEE/ASME Trans. Mechatronics*, vol. 28, no. 3, pp. 1268–1279, Jun. 2023.

[19] Y. Li, G. Lu, D. He, and F. Zhang, "Robocentric model-based visual servoing for quadrotor flights," *IEEE/ASME Trans. Mechatronics*, vol. 28, no. 4, pp. 2155–2166, Aug. 2023.

[20] Y. Chen et al., "Image-based visual servoing of unmanned aerial manipulators for tracking and grasping a moving target," *IEEE Trans. Ind. Informat.*, vol. 19, no. 8, pp. 8889–8899, Aug. 2023.

[21] K. Zhang, Y. Shi, and H. Sheng, "Robust nonlinear model predictive control based visual servoing of quadrotor UAVs," *IEEE/ASME Trans. Mechatronics*, vol. 26, no. 2, pp. 700–708, Apr. 2021.

[22] F. Chaumette and S. Hutchinson, "Visual servo control. I. Basic approaches," *IEEE Robot. Autom. Mag.*, vol. 13, no. 4, pp. 82–90, Dec. 2006.

[23] P. Serra, R. Cunha, T. Hamel, D. Cabecinhas, and C. Silvestre, "Landing of a quadrotor on a moving target using dynamic image-based visual servo control," *IEEE Trans. Robot.*, vol. 32, no. 6, pp. 1524–1535, Dec. 2016.

[24] D. Guo and K. K. Leang, "Image-based estimation, planning, and control for high-speed flying through multiple openings," *Int. J. Robot. Res.*, vol. 39, no. 9, pp. 1122–1137, Aug. 2020.

[25] J. Lin, Y. Wang, Z. Miao, H. Wang, and R. Fierro, "Robust image-based landing control of a quadrotor on an unpredictable moving vehicle using circle features," *IEEE Trans. Autom. Sci. Eng.*, vol. 20, no. 2, pp. 1429–1440, Apr. 2023.

[26] G. Wang, J. Qin, Q. Liu, Q. Ma, and C. Zhang, "Image-based visual servoing of quadrotors to arbitrary flight targets," *IEEE Robot. Autom. Lett.*, vol. 8, no. 4, pp. 2022–2029, Apr. 2023.

[27] A. Arif, H. Wang, H. Casta neda, and Y. Wang, "Finite-time tracking of moving platform with single camera for quadrotor autonomous landing," *IEEE Trans. Circuits Syst. I, Reg. Papers*, vol. 70, pp. 2573–2586, 2023.

[28] S. Yang, B. Xian, J. Cai, and G. Wang, "Finite-time convergence control for a quadrotor unmanned aerial vehicle with a slung load," *IEEE Trans. Ind. Informat.*, vol. 20, no. 1, pp. 605–614, Jan. 2024.

[29] X. Liang, P. Zhang, Y. Fang, H. Lin, and W. He, "Nonlinear control for aerial transportation systems with double-pendulum swing effects," *IEEE Trans. Ind. Electron.*, vol. 68, no. 7, pp. 6020–6030, Jun. 2021.

[30] X. Liang, H. Yu, Z. Zhang, H. Liu, Y. Fang, and J. Han, "Unmanned aerial transportation system with flexible connection between the quadrotor and the payload: Modeling, controller design, and experimental validation," *IEEE Trans. Ind. Electron.*, vol. 70, no. 2, pp. 1870–1882, Feb. 2023.

[31] T. Lee, M. Leok, and N. H. McClamroch, "Geometric tracking control of a quadrotor UAV on SE(3)," in *Proc. IEEE Conf. Decis. Control (CDC)*, Dec. 2010, pp. 5420–5425.

[32] T. Lee, "Robust adaptive attitude tracking on SO(3) with an application to a quadrotor UAV," *IEEE Trans. Control Syst. Technol.*, vol. 21, no. 5, pp. 1924–1930, Sep. 2013.

[33] F. A. Goodarzi, D. Lee, and T. Lee, "Geometric adaptive tracking control of a quadrotor unmanned aerial vehicle on SE(3) for agile maneuvers," *J. Dyn. Syst., Meas., Control*, vol. 137, no. 9, Sep. 2015, Art. no. 091007.

[34] M. Bisheban and T. Lee, "Geometric adaptive control with neural networks for a quadrotor in wind fields," *IEEE Trans. Control Syst. Technol.*, vol. 29, no. 4, pp. 1533–1548, Jul. 2021.

[35] H. K. Khalil, *Nonlinear Systems*. Upper Saddle River, NJ, USA: Prentice-Hall, 2002.

[36] F. Kendoul, "Nonlinear hierarchical flight controller for unmanned rotorcraft: Design, stability, and experiments," *J. Guid. Control Dyn.*, vol. 32, no. 6, pp. 1954–1958, 2009.

[37] B. Zhao, B. Xian, Y. Zhang, and X. Zhang, "Nonlinear robust adaptive tracking control of a quadrotor UAV via immersion and invariance methodology," *IEEE Trans. Ind. Electron.*, vol. 62, no. 5, pp. 2891–2902, May 2015.

[38] J. C. Johnson and R. W. Beard, "Globally-attractive logarithmic geometric control of a quadrotor for aggressive trajectory tracking," *IEEE Control Syst. Lett.*, vol. 6, pp. 2216–2221, 2022.

[39] V. Kumar and N. Michael, "Opportunities and challenges with autonomous micro aerial vehicles," *Int. J. Robot. Res.*, vol. 31, no. 11, pp. 1279–1291, Sep. 2012.

[40] R. Mahony, V. Kumar, and P. Corke, "Multirotor aerial vehicles: Modeling, estimation, and control of quadrotor," *IEEE Robot. Autom. Mag.*, vol. 19, no. 3, pp. 20–32, Sep. 2012.

Hai Yu (Student Member, IEEE) received the B.S. degree in automation from Jilin University, Changchun, China, in 2020. He is currently pursuing the Ph.D. degree in control science and engineering with the Institute of Robotics and Automatic Information System, Nankai University, Tianjin, China.

His research interests include the nonlinear control of unmanned aerial vehicles.

Jianda Han (Member, IEEE) received the Ph.D. degree in mechatronic engineering from Harbin Institute of Technology, Harbin, China, in 1998.

From 1998 to 2003, he was a Visiting Scientist with the City University of Hong Kong, Hong Kong; Michigan State University, East Lansing, MI, USA; and Cornell University, Ithaca, NY, USA. He is currently a Professor with the Institute of Robotics and Automatic Information System, Nankai University, Tianjin, China. His research interests include nonlinear estimation and control, robotics, and mechatronics systems.
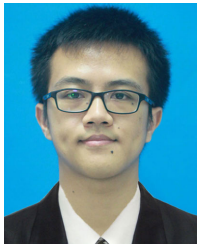
Zhaopeng Zhang received the B.S. degree in automation from Nankai University, Tianjin, China, in 2021, where he is currently pursuing the Ph.D. degree in control science and engineering with the Institute of Robotics and Automatic Information System.

His research interests include the nonlinear control of aerial manipulator systems.

Yongchun Fang (Senior Member, IEEE) received the B.S. and M.S. degrees in control theory and applications from Zhejiang University, Hangzhou, China, in 1996 and 1999, respectively, and the Ph.D. degree in electrical engineering from Clemson University, Clemson, SC, USA, in 2002.

From 2002 to 2003, he was a Post-Doctoral Fellow with the Sibley School of Mechanical and Aerospace Engineering, Cornell University, Ithaca, NY, USA. He is currently a Professor with the Institute of Robotics and Automatic Information System, Nankai University, Tianjin, China. His research interests include nonlinear control, visual servoing, the control of underactuated systems, and atomic force microscopy (AFM)-based nanosystems.

Dr. Fang received the National Science Fund for Distinguished Young Scholars of China. He was an Associate Editor of *Journal of Dynamic Systems, Measurement, and Control* (ASME).

Tengfei Pei received the B.S. degree in automation from Jilin University, Changchun, China, in 2022. He is currently pursuing the Ph.D. degree in control science and engineering with the Institute of Robotics and Automatic Information System, Nankai University, Tianjin, China.

His research interests include the motion planning of unmanned aerial vehicles.

Xiao Liang (Member, IEEE) received the B.S. degree in intelligence science and technology from Hebei University of Technology, Tianjin, China, in 2013, and the Ph.D. degree in control theory and control engineering from Nankai University, Tianjin, in 2018.

He is currently an Associate Professor with the Institute of Robotics and Automatic Information System, Nankai University. His research interests include motion planning and the nonlinear control of unmanned aerial vehicle systems.